UAB
Universitat Autònoma de Barcelona

Dipòsit digital de documents de la UAB

This is the **accepted version** of the journal article:

Guster, Bogdan; Pruneda, Miguel; Ordejon, Pablo; [et al.]. «Charge density waves and electron-hole instabilities of the hidden-nesting materials P4 W12 O44, - and -Mo4 O11». Physical review B, Vol. 110, Issue 9 (September 2024), art. 094103. DOI 10.1103/PhysRevB.110.094103

This version is available at https://ddd.uab.cat/record/307868

under the terms of the IN COPYRIGHT license

Charge density waves and electron-hole instabilities of the hidden-nesting materials $P_4W_{12}O_{44}$, γ- and η-Mo_4O_{11}

Bogdan Guster
Catalan Institute of Nanoscience and Nanotechnology, Campus Bellaterra, 08193 Barcelona, Spain and Q-Mat/CESAM, Université de Liège & European Theoretical Spectroscopy Facility, B-4000 Liége, Belgium

Miguel Pruneda and Pablo Ordejón
Catalan Institute of Nanoscience and Nanotechnology, Campus Bellaterra, 08193 Barcelona, Spain

Enric Canadell
Institut de Ciència de Materials de Barcelona (ICMAB-CSIC), Campus UAB, 08193 Bellaterra, Spain and Royal Academy of Sciences and Arts of Barcelona, Chemistry Section, La Rambla 115, 08002 Barcelona, Spain

Jean-Paul Pouget
Laboratoire de Physique des Solides, Université Paris-Saclay, CNRS, 91405 Orsay, France

The origin of the charge density wave instabilities in the isostructural but not isoelectronic octahedral layers of the three-dimensional (3D) solids γ-Mo_4O_{11} and $P_4W_{12}O_{44}$ is discussed on the basis of first-principles DFT calculations. These layers contain three different and superposed one-dimensional (1D) systems (two diagonal and one horizontal) associated with the three t_{2g} orbitals of the transition metal in octahedral coordination. Because of the special topology of the layers the three 1D systems are practically independent (hidden nesting) and the Lindhard function contains three different lines of intensity maxima associated with each of them. Clear cusps (six for $P_4W_{12}O_{44}$ and four for γ-Mo_4O_{11}) occur at the intersections of these intensity lines. The wave vector of the structural modulations associated with some of these cusps from our calculations is in good agreement with the observed CDW wave vectors. The nature of the different modulations is analyzed on the basis of the calculated thermal dependence of intra- and inter-chain coherence lengths of the diffuse lines associated with the diagonal and horizontal chains. Modulation in the diagonal chains is found to be more favorable than in the horizontal chain. The same type of wave vector is selected for γ-Mo_4O_{11} and $P_4W_{12}O_{44}$ despite having a different band filling. The coupling of the electronic instability to the phonon spectra and the relationship between the nature of the high temperature modulation with the width of the octahedral layers is discussed. Among the two Magnéli phases the inter-layer coupling is found to be somewhat stronger in η-Mo_4O_{11}. The relationship with other hidden nesting series of materials as the rare-earth tellurides is commented.

I. INTRODUCTION

The origin of the charge density wave (CDW) instabilities of low-dimensional materials is still the focus of much attention[1–4]. Essentially, two different types of mechanism dominate the scene. Weak electron-phonon coupling approaches generally provide an appropriate basis for discussing the CDWs of pseudo one-dimensional (1D) systems. However, those of materials with a higher dimensionality usually require strong electron-phonon coupling approaches. For a longtime, these studies have relied on model analytical treatments. However, the development of very efficient density functional theory (DFT) approaches during the last decades has completely changed the situation.[1] Both the electron-hole response and the phonon spectra of many of these solids can now be evaluated from first-principles DFT approaches and realistic microscopic mechanisms have been proposed based on the real crystal structures[5–8].

Molybdenum and tungsten oxides and bronzes have been for years at the forefront of this research[9,10]. For instance, the blue bronze $K_{0.3}MoO_3$ was one of the first materials to exhibit non linear conductivity due to the sliding of the CDW [11]. The detailed analysis of the nature of the CDWs in the potassium purple bronze KMo_6O_{17} led to the development of the so-called hidden-nesting concept[12]. Later, a DFT study of the wave-vector and temperature dependencies of the Lindhard response function of the blue bronze provided compelling evidence that the Peierls transition of this solid follows the weak electron-phonon coupling scenario in the adiabatic approximation, something that had not yet been proved for any material on the basis of first-principles calculations using the real crystal structure[5]. In that case, a clear microscopic mechanism was put forward and the CDW interchain coupling was proposed to occur through a Coulomb coupling between dipolar CDWs.

Under such circumstances the family of the monophosphate tungsten bronzes with pentagonal tunnels ($MPTB_p$)[13,14], $(PO_2)_4(WO_3)_{2m}$ with $m \geq 4$, acquires a special relevance. The different members of this family of perovskite related bronzes contain W-O octahedral metallic layers built with segments of m corner-sharing WO_6 octahedra. These layers are linked by PO_4 tetra-

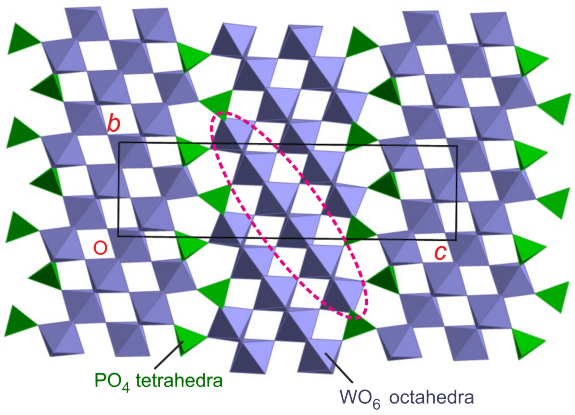

FIG. 1. Crystal structure of the m= 6 member of the $MPTB_p$ family, $P_4W_{12}O_{44}$. The green and blue units are the PO_4 tetrahedra and WO_6 octahedra, respectively. The segment of m= 6 octahedra making the repeat unit of the W-O layer is highlighted.

hedra (see Fig. 1 for the m= 6 member, i.e. $P_4W_{12}O_{44}$). The crystal structure of the γ-Mo_4O_{11} Magnéli phase[15] is built from MoO_6 octahedra and MoO_4 tetrahedra and is isostructural with the m= 6 member of the $MPTB_p$ family[16]. Both γ-Mo_4O_{11}[17] and the $MPTB_p$ phases[18] exhibit resistivity anomalies associated with CDW originating from the partially filled t_{2g}-block bands of their perovskite-type octahedral layers.[19] At this point let us note the existence of another Magnéli phase, η-Mo_4O_{11}[15], built from the same W-O layers and PO_4 tetrahedra but with a slightly different link between layers (see Fig. S3 of the Supplementary Information (SI)), which also exhibits resistivity anomalies.[20,21]

The nature of the CDW instability in the $MPTB_p$ has been extensively studied by X-ray diffuse scattering[20,22,23]. As for the blue bronze[5], the essential instability is of ferroelectric type consisting on a shift of the tungsten atoms inside each individual segment of m octahedra. However, structural refinements pinpoint an important difference between the low and high m members of the family. Whereas the W shift inside the octahedra is small and similar to those found in the blue bronze for the low m members ($u_W^{m=4} \sim 0.04$ Å[24] and $u_W^{m=6} \sim 0.04$ Å[25]), it is very large for the high m members ($u_W^{m=8} \sim 0.23$ Å[25] and $u_W^{m=10} \sim$ 0.2-0.3 Å[25,26]). This observation immediately suggests a change in the CDW mechanism along the series, which is a unique feature among CDW materials of the same family. Another appealing aspect is the possibility to study the electron filling dependence of the CDW mechanism. As mentioned, the γ-Mo_4O_{11} Magnéli phase is isostructural with the m= 6 member of the $MPTB_p$ family. The formal oxidation state of P in the PO_4 tetrahedra of the $MPTB_p$ phases is +5, while that of Mo in the MoO_4 tetrahedra of γ-Mo_4O_{11} is +6 whereas Mo and W belong to the same group of the periodic table and have both 6 valence electrons. Consequently, the partially filled t_{2g} bands of the Magnéli phase have more d electrons (4 per repeat unit of the layer) than do the W-O layers of the corresponding m= 6 $MPTB_p$ phase (2 electrons per repeat unit of the layer. This point is developed in more detail in Fig. S2). Thus, the electronic instabilities of the Mo-O and W-O layers are expected to differ.

$P_4W_{12}O_{44}$ exhibits three CDW transitions at 120 K, 60 K and ∼30 K associated with the appearance of superlattice spots at 0.3825a*, (0.3099a*+0.2908b*) and (0.26a*+0.07b*)[20,22,25] respectively (the ab planes are those associated with the conducting layers). Only those at 120 K and 60 K are visible in the resistivity measurements. η- and γ-Mo_4O_{11}, with bc conducting planes, suffer a CDW modulation at 109 K and 100 K, respectively, with wave vector ∼0.23b*.[20,21,27] η-Mo_4O_{11} exhibits another CDW at ∼30 K with wave vector (0.552a*, 0.47b*, 0.30c*).[20,21] The three compounds keep their metallic character after the CDW modulations.

The crystal structures of the blue bronze, the γ- and η-Mo_4O_{11} Magnéli phases and the $MPTB_p$ family are all built from corner-sharing octahedral clusters[15,16] and the Fermi surface (FS) originates from the bottom part of the t_{2g}-block bands[19]. Both experimental and theoretical studies suggest that the CDW anomalies of the m=4 member of the $MPTB_p$ family ($P_4W_8O_{32}$) may be well accounted for by a weak electron-phonon coupling mechanism.[22,28] Bearing in mind our previous work on the blue bronze,[5] we decided to carry out a study of the Lindhard response of $P_4W_{12}O_{44}$ as well as the γ- and η-Mo_4O_{11} Magnéli phases. Note that in contrast with the blue bronze, $P_4W_{12}O_{44}$ and the Mo_4O_{11} Magnéli phases exhibit an almost isotropic 2D metallic behavior.[14,17] Because of the isostructural character of $P_4W_{12}O_{44}$ and γ-Mo_4O_{11} we will be able to discuss how the different filling of the t_{2g}-block bands affects the CDW instability. Another aspect that we will discuss is how the different connection between layers (and segments of octahedra) affects the CDW instability. In a forthcoming work we will examine the change in the CDW mechanism along the $MPTB_p$ family. We hope that the set of studies concerning the blue bronze, the Mo_4O_{11} Magnéli phases and selected members of the $MPTB_p$ family will provide a clear and comprehensive landscape of the CDW instability in transition metal oxides and bronzes.

II. COMPUTATIONAL DETAILS

The DFT calculations[29,30] were carried out using a numerical atomic orbitals DFT approach implemented in the SIESTA code[31–33]. The Perdew-Burke-Ernzerhof (PBE) functional was used to account for the exchange-correlation energy[34]. The core electrons have been replaced by norm-conserving scalar relativistic pseudopotentials[35] factorized in the Kleinman-Bylander form[36]. We have used a split-valence double-ζ basis set including

polarization functions[37]. In all calculations, we use a cut-off of 350 Ry for the real space integrals, and a tolerance of 10^{-4} and 10^{-3} eV on the density matrix and the total energy, respectively, for the convergence of the SCF cycle. To sample the Brillouin zone (BZ) for the electronic states, a Monkhorst-Pack[38] k-points grid of 27×27×15 was used for the non-distorted unit cell and scaled accordingly to the supercell calculations. The Lindhard electron-hole response function, which in the plane wave approximation reads[1]

$$\chi(q) = -\sum_{i,j}\sum_{k} \frac{f_F(\epsilon_i(k)) - f_F(\epsilon_j(k+q))}{\epsilon_i(k) - \epsilon_j(k+q)}, \qquad (1)$$

where f_F is the Fermi-Dirac distribution function, was obtained from the computed DFT band eigenvalues $\epsilon_i(k)$. The integral over k-points of the BZ was approximated by a direct summation over a dense, regular grid of points. As the Lindhard function is more sensitive to the accuracy of the BZ integration than the total energy, the k-points grid used for its calculation must be more dense than in the standard self-consistent determination of the charge density and Kohn-Sham energy. The calculations are done using the eigenvalues obtained in the DFT calculation for the coarser grid, and interpolating their values in the denser grid, using a post-processing utility available within the SIESTA package. In this work the BZ was sampled using a grid of (200×200×10) k-points, for the calculation of the Lindhard response function.

III. STRUCTURAL VS ELECTRONIC DIMENSIONALITY: LAYERS WITH THREE PSEUDO-INDEPENDENT CHAINS

As can be see in Figs. 1 and 2a, the octahedral layers in $MPTB_p$ can be described as stepped layers where every step is an infinite chain along the a direction with m octahedra in the repeat unit. Since the crystal structures of $P_4W_{12}O_{44}$ and γ-Mo_4O_{11}[15,16] use axes with different labeling, in this work we will follow the system of axes shown in Figs. 1 and 2a for $MPTB_p$: the intra-step and inter-steps directions will be refereed to as a and b, respectively. In order to fully grasp the nature of the different anomalies in the octahedral layers of $P_4W_{12}O_{44}$ and γ-Mo_4O_{11} it is essential to realize that these layers should be viewed as the superposition of three different types of octahedral chains[19]. As graphically shown in Fig. 2a, these chains run along the a, (a+b) and (a-b) directions of the layer. The chains along the (a+b) and (a-b) directions are equivalent but different from the chains running along a.

The reason why it is important to realize this structural feature is because a transition metal centered MO_6 octahedra possesses three equivalent t_{2g} orbitals (see Fig. 2b) which are contained in the planes of the three mentioned chains (i.e., those defined by the "equatorial" O atoms) running along the a, (a+b) and (a-b) directions. These

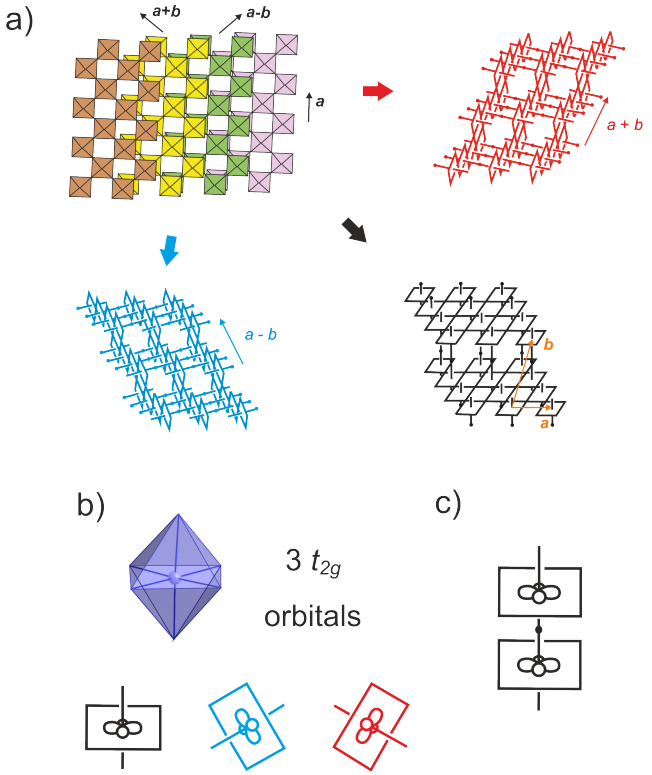

FIG. 2. (a) Schematic illustration of the occurrence of three different types of chains along the a, (a+b), and (a-b) directions in the octahedral layers of the $MPTB_p$. For simplicity we have shown the case for m= 4. (b) The three t_{2g} orbitals of a transition metal centered MO_6 octahedron (c) Illustration of the δ-type connection between octahedra in parallel chains.

are the black, red and blue t_{2g} orbitals of Fig. 2b. These orbitals make the usual π-type interactions in perovskite type materials with the appropriate O p orbital along the chain direction, thus leading to dispersive bands. The important feature is that these t_{2g} orbitals are also of δ type along the inter-chain direction connecting parallel chains and thus can not mix with O p orbitals of these chain interconnecting sites. Thus, from the electronic viewpoint the parallel chains behave independently. Because of the local orthogonality of the three t_{2g} orbitals the interaction of the three types of dispersive bands is also very weak. Consequently, as far as the nature of the lower partially filled bands of the $MPTB_p$ are concerned, they can be considered as resulting from the weak hybridization of three 1D bands running along the a, (a+b) and (a-b) directions.[12,19] Except when otherwise stated we will refer to the two chains running along the $a \pm b$ directions as "diagonal" and that running along the a direction as "horizontal".

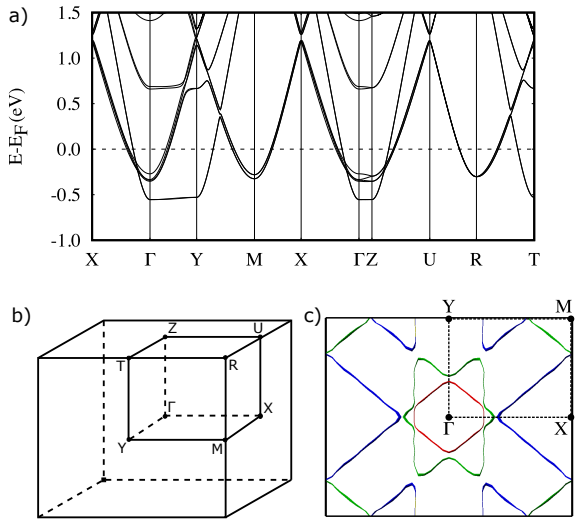

FIG. 3. Band structure (a), schematic Brillouin Zone (b) and Fermi surface viewed along the c^* direction (c) for $P_4W_{12}O_{44}$. Γ= (0, 0, 0), X= (1/2, 0, 0), Y= (0, 1/2, 0), Z= (0, 0, 1/2), M= (1/2, 1/2 0), U= (1/2, 0 1/2), R= (1/2, 1/2,1/2) and T= (0, 1/2, 1/2) in units of the reciprocal lattice vectors.

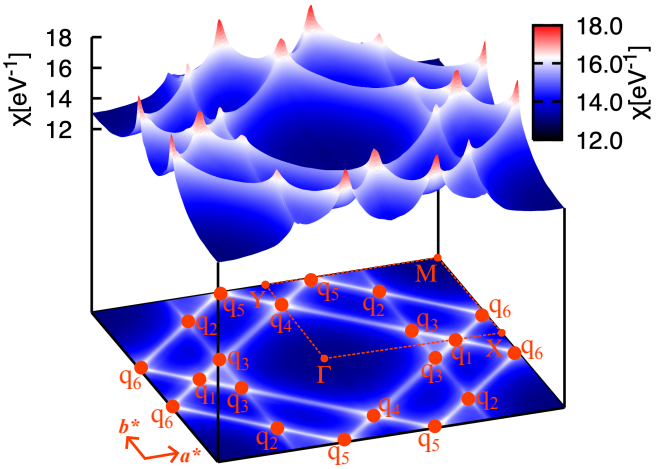

FIG. 4. Plot of the Lindhard response function calculated for $P_4W_{12}O_{44}$ in the (a^*,b^*) reciprocal plane at 10 K.

IV. ELECTRONIC STRUCTURE OF $P_4W_{12}O_{44}$

The band structure and Fermi surfaces (FS) for $MPTB_p$ are well known[19,28,39,40]. Those for the $m = 6$ member of the series according to the present DFT study are shown in Fig. 3a and c, respectively. The Fermi level cuts three pairs of almost degenerate bands because there are two layers per unit cell. The fact that these bands are practically degenerate indicates that the inter-layer interactions are almost nil (see the very small band dispersion along the interlayer direction (i.e. Γ to Z in Fig. 3a). The occurrence of one pair of 1D bands along the a^* direction is clear in Fig. 3a (see the lower pair of bands in the X-Γ-Y traject). As expected from the structural analysis of the previous section and these results, the FS of Fig. 3c can be considered to result from the weak hybridization of the FS (i.e. pairs of parallel planes) of three 1D systems along the a, a+b and a-b directions.

The octahedral W-O layers of $P_4W_{12}O_{44}$ contain three different chains of two different types: (1) one chain along a and (2) two chains of the same type along (a+b) and (a-b). Since the partially filled t_{2g} bands contain 2 electrons, it is interesting to have a hint on how these electrons are distributed among the three different chains. Because of the hidden 1D nature of the bands there is a simple way to have a good estimation. Let us refer to the band occupation (from 0 to 1) of the bands associated with the chains along the a, (a+b) and (a-b) directions as Ω_a, Ω_{a+b} and Ω_{a-b}, respectively. It is clear that $\Omega_{a+b} = \Omega_{a-b} = 1/2(1-\Omega_a)$, since the total number of electrons in one layer is 2 and the chains along (a+b) and (a-b) are equivalent. Since $\Omega_a = 2k_F^a/a^*$ it follows that $\Omega_{a+b} = \Omega_{a-b} = 1/2 - k_F^a/a^*$. From the FS of $P_4W_{12}O_{44}$ (Fig. 3c) it can be estimated that $k_F^a/a^* \simeq 0.14$ so that 0.56 electrons are associated with the chains along a and 0.72 electrons are associated with each of the chains along the diagonal ($a \pm b$) directions. Consequently the conduction electrons are unevenly distributed among the three chains, with the diagonal chains being more populated.

V. QUANTITATIVE ANALYSIS OF THE LINDHARD RESPONSE FUNCTION OF $P_4W_{12}O_{44}$

The first-principles Lindhard function for $P_4W_{12}O_{44}$ at 10 K is shown in Fig. 4. The occurrence of three different pairs of lines of intensity maxima perpendicular to the a^* and ($a^* \pm b^*$) directions is clearly shown, as expected from the hidden nesting mechanism. In fact the two types of diffuse lines are already clearly visible at 300 K (see Fig. S1). Clear cusps occur at the crossing points of these lines. Six of them, q_i (i=1-6), are symmetry inequivalent and are related to possible CDWs. A comparison of Figs. 4 and S1 shows that the q_i singularities broaden considerably upon heating in the directions of the crossing lines which define these singularities. This aspect will be further developed in Sect. V C. In the next subsections we explore the temperature and wave vector dependence of this complex Lindhard function and later we will discuss the relevance of these results to understand the nature of the CDWs exhibited by $P_4W_{12}O_{44}$.

A. Scans along the a^* direction

Shown in Figs. 5a and b are scans of the Lindhard function along the a^* direction. In both cases there are two

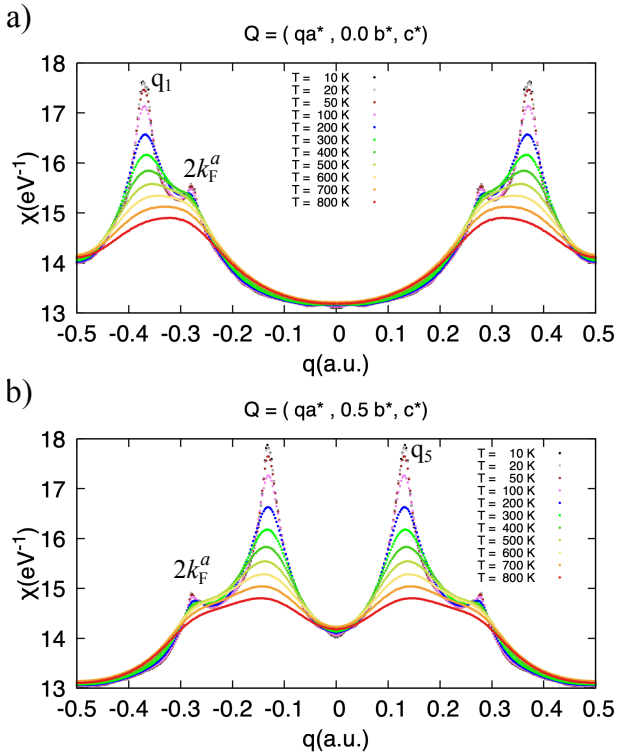

FIG. 5. Thermal dependence of scans along a^* of the Lindhard function for $P_4W_{12}O_{44}$.

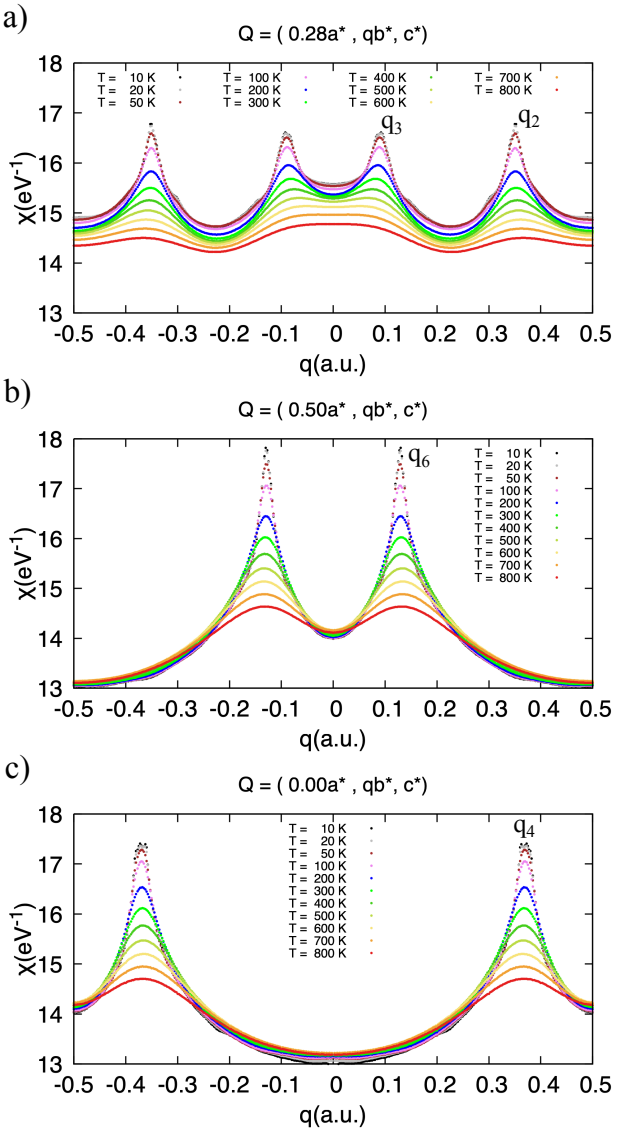

FIG. 6. Thermal dependence of scans along b^* of the Lindhard function for $P_4W_{12}O_{44}$.

maxima although only one of them is really significant. The small maximum appears in both figures at $0.28a^*$ which, as discussed above, corresponds to the $2k_F$ value for the 1D band of octahedral chains along the a direction ($2k_F^a$).Thus, it corresponds to the intra-band nesting associated with the horizontal chains. When the b^* component is fixed at the value 0.0 (Fig. 5a) a strong maximum appears at $0.38a^*$. As shown in Fig. 4 this maximum (q_1) occurs at the crossing of *two* diagonal maxima intensity lines each one being associated with the intra-band nesting of the 1D band of one diagonal chain. Consequently, the intensity at this point is very strong compared with that at $2k_F^a$. This abrupt maxima of the Lindhard function corresponds to the simultaneous nesting of the 1D bands associated with the *two* diagonal directions. Thus, a single modulation with wave vector $q_1 = 0.38a^* + 0.00b^*$ will open gaps in very large parts of the diagonal components of the FS. When heating, the response becomes wider and finally overlaps with the smaller response of the intra-band nesting of the horizontal chain, $2k_F^a$. When the b^* component is fixed at the 0.5 b^* value (Fig. 5b) we find again the small peak associated with $2k_F^a$ and another strong peak, even a little bit more intense than q_1, at $q_5 = 0.13a^* + 0.50b^*$. Again, looking at Fig. 4 it is clear that this maxima occurs at the crossing of *two* diagonal maxima intensity lines and it is thus associated with a CDW affecting the diagonal chains and opening gaps in large portions of the diagonal components of the FS.

B. Scans along the b^* direction

Shown in Figs. 6a, b and c are scans of the Lindhard function along the b^* direction for fixed a^* values of 0.28 (i.e. where the maxima intensity line of the 1D band of the horizontal chain lies), 0.50 and 0.00. In the first case two different sharp maxima occur at $q_2 = 0.28a^* + 0.35b^*$ and $q_3 = 0.28a^* + 0.09b^*$. These maxima occur (see Fig. 4) at the crossing of *two* maxima intensity lines associated with 1D bands of diagonal and horizontal chains. The two maxima are thus associated with CDW opening gaps in large portions of the horizontal and one of the diagonal components of the FS. Note that these peaks have an intensity noticeably smaller than those of q_1 and q_5. This observation, together with the small intensity of the peak for $2k_F^a$ clearly suggests that the horizontal chains

are less effective than the diagonal chains in lowering the energy of the system through a modulation of their electrons. For the scans at fixed $0.50a^*$ a sharp and very intense peak at $q_6 = 0.50a^* + 0.13b^*$ occurs. This peak is associated with the crossing of *two* diagonal maxima lines so that it is associated with a CDW involving the two diagonal chains. Finally, the scans at fixed $0.00a^*$ exhibit a sharp peak at $q_4 = 0.00a^* + 0.38b^*$, at the crossing of the *two* diagonal maxima intensity lines with the b^* axis. It thus corresponds to a CDW associated with the two diagonal chains in-phase along the b^* direction. The intensity of this peak is intermediate between those of the $q_1/q_5/q_6$ and q_2/q_3 ones.

C. The full Lindhard function

The first-principles Lindhard function of $P_4W_{12}O_{44}$ contains two different types of lines of intensity maxima perpendicular to either the a (i.e. horizontal chains) or $(a \pm b)$ (i.e. diagonal chains) directions and six different clear cusps at the intersections of two of these lines. Such cusps point out the possibility of different CDWs stabilizing the modulated structure. Four of these modulations are associated with the diagonal chains (q_1, q_4, q_5 and q_6) and two with one of the diagonal chains and the horizontal chain (q_2 and q_3). These modulations can be classified into three different groups when considering not only the chain location but the commensurate vs incommensurate nature of the modulation:
- (1) modulations of the two diagonal chains with one incommensurate component along a: q_1 and q_5. Note that q_1 is in-phase along b whereas q_5 is out-of-phase.
- (2) modulations of the two diagonal chains with one incommensurate component along b: q_4 and q_6. Note that q_4 is in-phase along a whereas q_6 is out-of-phase.
- (3) doubly incommensurate modulations of one diagonal chain and one horizontal chain: q_2 and q_3.

From the six potential modulations suggested by our calculations only three are experimentally achieved. The three CDWs of $P_4W_{12}O_{44}$ occurring successively at 120 K, 60 K and 30 K have been experimentally characterized by X-ray diffuse scattering measurements. They are associated with the appearance of superlattice spots at $0.3825(2)a^*$, $(0.3099(4)a^* + 0.2908(3)b^*)$ and $(0.26a^* + 0.07b^*)$, respectively.[20,22,25] Comparing these values with the six cusps of the Lindhard function it appears that the transition at 120 K should be associated with q_1, that at 60 K with q_2 and that at 30 K with q_3. Consequently, from the four modulations of the diagonal chains only one is selected by the system, q_1, and is responsible for the high temperature CDW.

Note that even if the six peaks exhibit a strong intensity those associated with the two diagonal chains (q_1, q_4, q_5 and q_6) are those with the stronger intensity. Those associated with one diagonal and one horizontal chains (q_2 and q_3) have weaker intensity and however seem to be selected for the low temperature CDW. That only one of the four strong intensity peaks is selected at high temperature is a strong indication of the important role of the inter-chain (see Fig. 8c) and electron-phonon coupling in selecting the kind of modulation affording the maximum stabilization to the system. As a matter of fact, the wave vector of the modulation selected here (q_1) is not far from that responsible for the antiferroelectric (AF) high-temperature order of WO_3.[41]

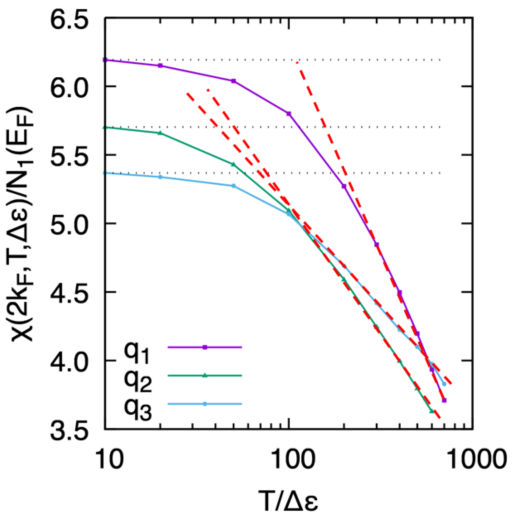

FIG. 7. Thermal dependence of the $2k_F$ peak intensity for the three different electron-hole responses q_i (i=1,2,3) of $P_4W_{12}O_{44}$. The red dashed lines outline the high temperature $\ln(C/T)$ dependence of the q_i (i= 1, 2 and 3) peaks.

Before considering in more detail the structural and electronic factors selecting the three q_i's among the six suggested by the electron-hole response we must have a deeper understanding of the calculated Lindhard function. The thermal dependence of the $2k_F$ peak intensity for the three different electron-hole responses is reported in Fig. 7. They exhibit the expected Peierls-type logarithmic divergence at high temperature and a saturation at lower temperatures. The q_1, q_2 and q_3 peak intensities saturate around 100 K, 50 K and 60 K, not far from the respective transition temperatures, T_{P1}= 120 K, T_{P2}= 60 K and $T_{P3} \sim$ 30 K. The saturation most likely occurs because of multiple inter-chain different responses which overlap, preventing a full divergence of a single electronic response.

The coherence lengths associated with the two different types of diffuse lines perpendicular to either the a (i.e. horizontal chains) or $(a \pm b)$ (i.e. diagonal chains) directions, can be obtained from longitudinal (i.e. perpendicular to the $2k_F$ line) and transverse (i.e. along the $2k_F$ line) scans of the Lindhard function (see Fig. 8c). The inverse intra-chain coherence lengths (i.e. the half-width at half-maximum (HWHM) of the electron-hole response function) for the vertical and diagonal diffuse lines are reported in Fig. 8a. From the 0 K values, intra-chain coherence lengths of $\sim$40 and $\sim$50 Å can be estimated for the

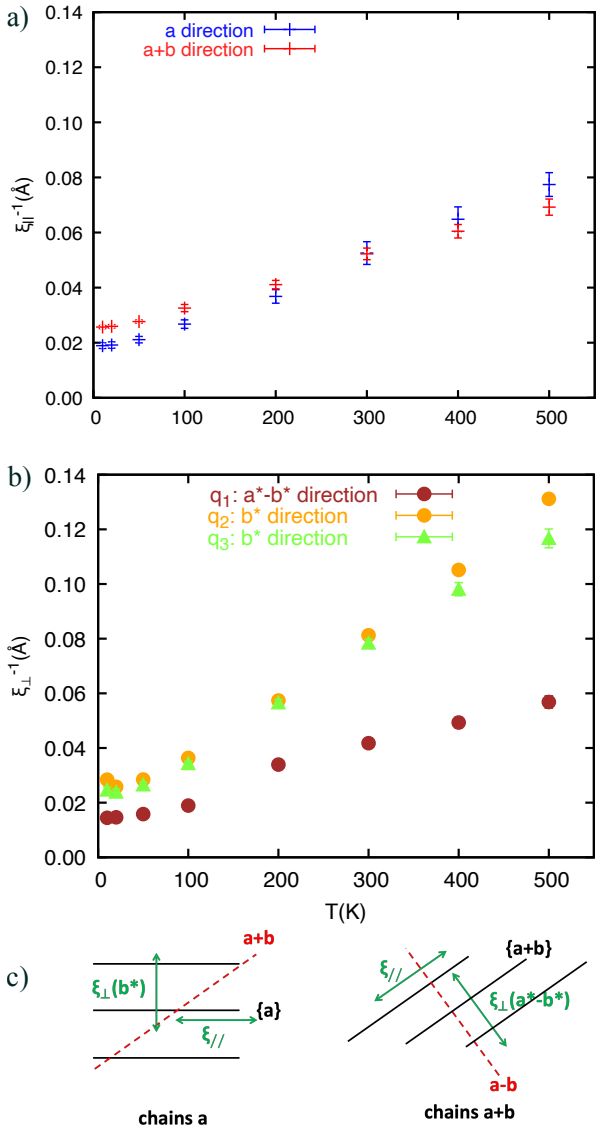

FIG. 8. Thermal dependence of the intra-chain (a) and inter-chain (b) electron-hole coherence length of the horizontal and diagonal chains calculated for the q_1, q_2 and q_3 singularities of $P_4W_{12}O_{44}$.(c) Definition of the different coherence lengths. The continuous black and dashed red lines represent the directions of the chains in the structure which are perpendicular to the associated diffuse lines.

diagonal and horizontal chains, respectively. These values are about two and three times larger than $\lambda_{2k_F}(a) \cong 19$ Å so that the $2k_F$ modulation wave is spatially well defined.

For a Peierls system the slope of the inverse electron-hole coherence length as a function of temperature is related to the inverse Fermi velocity through the relation $\xi_{\parallel}^{-1} = \pi k_B T/\hbar v_F$.[1] From the values in Fig. 8a it is found that v_F is around 1.75 and 1.50 eV·Å for the horizontal and diagonal directions. A slightly lower value, 1.2 eV·Å, can be estimated for v_F along the horizontal direction from ARPES data.[42] Note that the v_F value for the $K_{0.3}MoO_3$ blue bronze estimated from the same type of calculations is 2 eV·Å,[5] which is not far from these values although the type of octahedral chains is somewhat different.

The inverse intra-chain coherence lengths $\xi_{\parallel}^{-1}$ for the two types of chains are not very different and comparable to that of the blue bronze.[5] In contrast, the inverse inter-chain coherence lengths $\xi_{\perp}^{-1}$ are noticeably smaller. Fig. S1 shows the square-like broadening of q_i for the Lindhard response at 300 K. For instance, $\xi_{\perp}^{-1}$ at 300 K is 0.08 Å^{-1} for the q_2 and q_3 peaks and 0.04 Å^{-1} for the q_1 peak of $P_4W_8O_{32}$. However, at the same temperature $\xi_{\perp}^{-1}$ for the blue bronze is 0.2 Å^{-1}. This means that, compared with a conventional Peierls type system as the blue bronze, where the coupling occurs in a bunch of separated parallel chains, the inter-chain coupling is considerably more efficient in $P_4W_8O_{32}$.

In the hidden-nesting materials the different chains differ by the nature of the orbitals leading to the 1D behaviour but they spatially superpose. However, in the conventional systems the chains are spatially separated and the inter-chain coupling, which is essentially of Coulomb type,[1] is less efficient. Since the different chains in the present system form part of the same layer, one could think that transfer integral mediated interactions between the different sets of parallel chains could be important. At this point it is useful to point out a difference with another family of CDW materials: the rare-earth tellurides.[43,44] Although the real mechanism behind their CDW instability is still not completely clear,[1] Yao *et al*[45] discussed their CDW instabilities from the viewpoint of hidden-nesting. Using tight-binding arguments, they showed that warping of the 1D FSs would lead to a change of the nesting vector as a function of temperature. However, as shown by the different scans in Figs. 5 and 6, in $P_4W_{12}O_{44}$ the different q_i maxima of the Lindhard function do not change with temperature. This simply means that the hidden 1D chains are strictly 1D (i.e. except for a very weak interaction at the crossing points, the FS components are very flat and thus transfer integral mediated inter-chain interactions between parallel chains do not play any significant role). In other words, the CDW in a given chain of $P_4W_{12}O_{44}$ must interact with parallel chains either by direct Coulomb interactions, or indirectly via the polarization induced by an oblique chain, as illustrated in Fig. 8c.

In fact, $\xi_{\perp}^{-1}$ of peak q_1 is considerably smaller than those for q_2 and q_3 and is even smaller than the intra-chain one. This means that the polarization mechanism must be very important and that from the two types of coupling between oblique chains: (*i*) that involving two diagonal chains and (*ii*) that involving one diagonal and one horizontal chains, the first one is considerably more efficient. Thus the CDW instability of the diagonal chains seems to be very efficient in extending the modulation along the layer and more likely governs the CDW formation in this material. At first sight, this

could be considered to be the reason why q_1 is selected by the system as the high temperature CDW. However, we stress the fact that up to now we have only considered the purely electronic aspects. Especially in a 3D lattice as that of $P_4W_{12}O_{44}$ the strain generated by the periodic lattice distorsion should be considered.

VI. ELECTRONIC STRUCTURE OF THE MAGNÉLI PHASES γ- AND η-MO_4O_{11}

The calculated band structures and FS for γ- and η-Mo_4O_{11} are shown in Fig. 9. Note that the axes of the crystal structure[46,47] are interchanged with respect to those of $P_4W_{12}O_{44}$; in γ-Mo_4O_{11} a is the inter-layer direction, c is the direction of the horizontal chains and thus the diagonal chains run along the $b \pm c$ directions. However, for easiness of the comparison we have kept the same labeling used in the previous sections. Also note that whereas γ-Mo_4O_{11} is orthorhombic as $P_4W_{12}O_{44}$, η-Mo_4O_{11} (see Fig. S3a) is monoclinic[47] (hence the small difference in the projection views of the two FS). Except for the higher lying Fermi level in the BS and the concomitant shift of the vertical hidden line in the FS due to the larger band filling, these results are very similar to those for $P_4W_{12}O_{44}$. At this stage no major difference can be appreciated among the two Magnéli phases (but see below). Since these FS can be considered again as the superposition of three 1D systems, $\Omega_a = 2k_F^a/a^* = 0.50$ and $\Omega_{a+b} = \Omega_{a-b} = 1 - k_F^a/a^* = 0.75$ so that the number of electrons in the horizontal chain is 1 and those in anyone of the two diagonal chains is 1.5. Consequently, the diagonal chains have been more strongly populated with respect to $P_4W_{12}O_{44}$ and the uneven distribution of electrons between the chains has increased (see Fig. S2). The nature of the different bands and FS has been analyzed in detail elsewhere.[48]

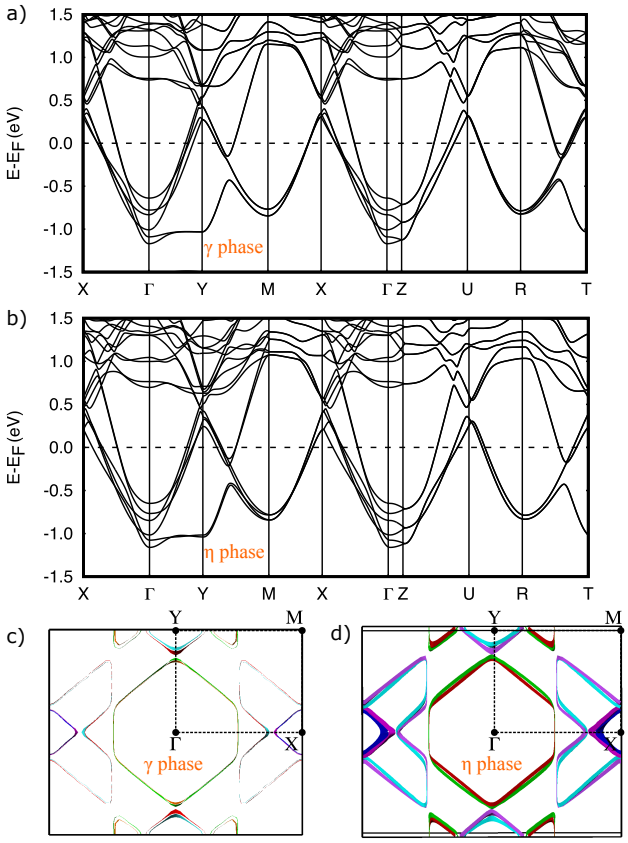

FIG. 9. Band structure and Fermi surface viewed along the a^* direction for γ-Mo_4O_{11} (a and c) and η-Mo_4O_{11} (b and d). Γ= (0, 0, 0), X= (1/2, 0, 0), Y= (0, 1/2, 0), Z= (0, 0, 1/2), M= (1/2, 1/2 0), U= (1/2, 0 1/2), R= (1/2, 1/2,1/2) and T= (0, 1/2, 1/2) in units of the reciprocal lattice vectors. Comparison between parts c and d reveals an enhanced splitting of the FS for the η phase

VII. QUANTITATIVE ANALYSIS OF THE LINDHARD RESPONSE FUNCTION OF THE MAGNÉLI γ-MO_4O_{11} PHASE

The first-principles Lindhard function for γ-Mo_4O_{11} is shown in Fig. 10. The occurrence of lines of intensity maxima perpendicular to the a^* and ($a^* \pm b^*$) directions are again clearly seen. Note that the center of the plot in Fig. 10 has been shifted to the M point so as to make visible the line perpendicular to a^* passing throught this point. Clear cusps occur at the crossing points of the lines of intensity maxima.

Shown in Fig. 11 is a scan of the Lindhard function along the (a^*+b^*) diagonal direction. Successive intensity maxima occur at $q_1 = 0.25a^*$, $q_2 = 0.25b^*$, $q_3 = 0.50a^* + 0.25b^*$ and $q_4 = 0.25a^* + 0.50b^*$. The q_3 maxima is the strongest because it occurs at the crossing of three intensity lines; the q_1, q_2 and q_4 maxima have practically the same intensity and occur at the crossing of two

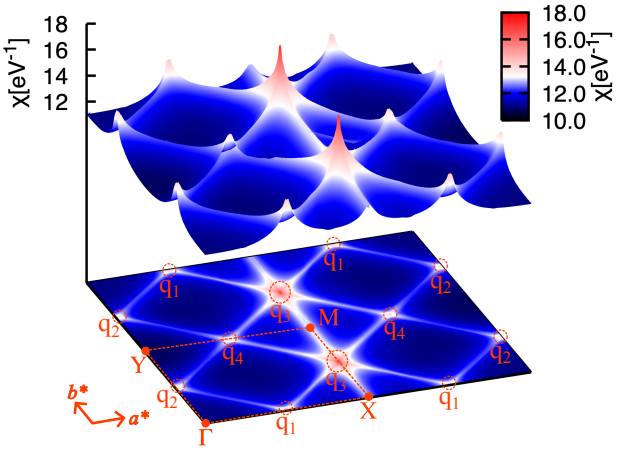

FIG. 10. Lindhard response function calculated for γ-Mo_4O_{11} in the (a^*,b^*) reciprocal plane at 10 K.

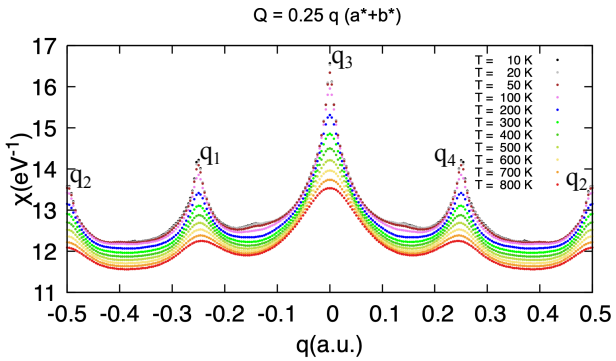

FIG. 11. Thermal dependence of scans along the diagonal direction a^*+b^* of the Lindhard function for γ-Mo_4O_{11}.

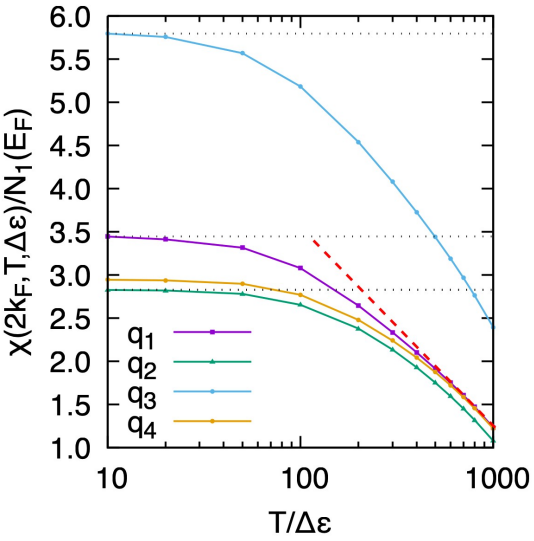

FIG. 12. Thermal dependence of the $2k_F$ peak intensity for the different electron-hole responses q_i (i=1,2,3,4) of γ-Mo_4O_{11}. The dashed line shows the high temperature $\ln(C/T)$ dependence of the q_2 peak

diagonal intensity lines.

The main difference with the situation for $P_4W_{12}O_{44}$ is that the additional pair of electrons lead to a half-filling of the band associated with the horizontal chain thus shifting the associated vertical maxima intensity line to the border of the BZ. Thus, two of the maxima in the Lindhard function of $P_4W_{12}O_{44}$ occurring at the crossing of the maxima intensity lines of the diagonal and horizontal lines, q_1 and q_3, do not occur for γ-Mo_4O_{11} and the only maxima implicating the horizontal chains is q_3. The three maxima associated with the two diagonal lines are the same as those of $P_4W_{12}O_{44}$ except that now all the wave vector components are commensurate. When heating, the responses becomes wider but remain centered at the same wave vector.

Only one of the four potential modulations suggested by our calculations is experimentally achieved, giving again a strong indication of the importance of the electron-phonon coupling in imposing the kind of modulation providing the stronger stabilization to the system. This is the q_1 maxima that in terms of the actual crystal structure cell axes of γ-Mo_4O_{11} is q= $0.25b^*$, in good agreement with the experimental one, $\sim 0.23b^*$. The thermal dependence of the $2k_F$ peak intensity for the different electron-hole responses is reported in Fig. 12. They exhibit the expected Peierls-type logarithmic divergence at high temperature and a saturation at lower temperatures. The q_1 peak intensities saturate around 110 K close to its transition temperatures, $T_P \sim$ 110 K. Note that this q_1 maxima corresponds to the q_1 maxima for $P_4W_{12}O_{44}$, which is the wave vector of the observed high temperature modulation.

From the 0 K values intra-chain coherence lengths of $\sim$40 and $\sim$25 Å can be estimated for the diagonal and horizontal chains, respectively. Again, these values show that the $2k_F$ modulation wave is spatially well defined. Note, however, that, in contrast with $P_4W_{12}O_{44}$, the intra-chain coherence length of the diagonal chains is clearly larger than that of the horizontal chains. From the values in Fig. 13 it is found that v_F is 1.5 and 2.6 eV·Å for the horizontal and diagonal directions. The notably larger coherence length values for the diagonal chains are in agreement with the fact that the horizontal chains are not involved in the CDW of γ-Mo_4O_{11}.

That the same type of wave vector is again selected among those highlighted by the Lindhard function despite the difference in band filling is again a strong suggestion of the importance of the electron-phonon coupling. The effectiveness of the different periodic lattice distortions in lowering the energy of the system is only accurately taken into account through the so-called structured susceptibility, $D_2(q)$.[1,49,50] Since γ-Mo_4O_{11} and $P_4W_{12}O_{44}$ are isostructural, it is not expected that the strain generated by the different modulations changes considerably for the two compounds. We thus conclude that the band filling changes the actual wave vector but not the direction of the high temperature CDW in the two compounds.

A similar analysis of the Lindhard response of η-Mo_4O_{11} has been carried out. Most of the results, which are quite similar to those for γ-Mo_4O_{11}, are summarized in Figs. S4-S7.

VIII. COUPLING OF THE ELECTRONIC INSTABILITY TO THE PHONON SPECTRA IN $P_4W_{12}O_{44}$ AND γ-MO_4O_{11}

The electronic Lindhard response for $P_4W_{12}O_{44}$ and γ-Mo_4O_{11} (Figs. 4 and 10) reveals many sharp maxima of $\chi(q)$. Among them, those at the q_1 reciprocal position corresponds to their upper CDW transition observed. However, these wave vectors are not those where the Lindhard response is the strongest. This means that the

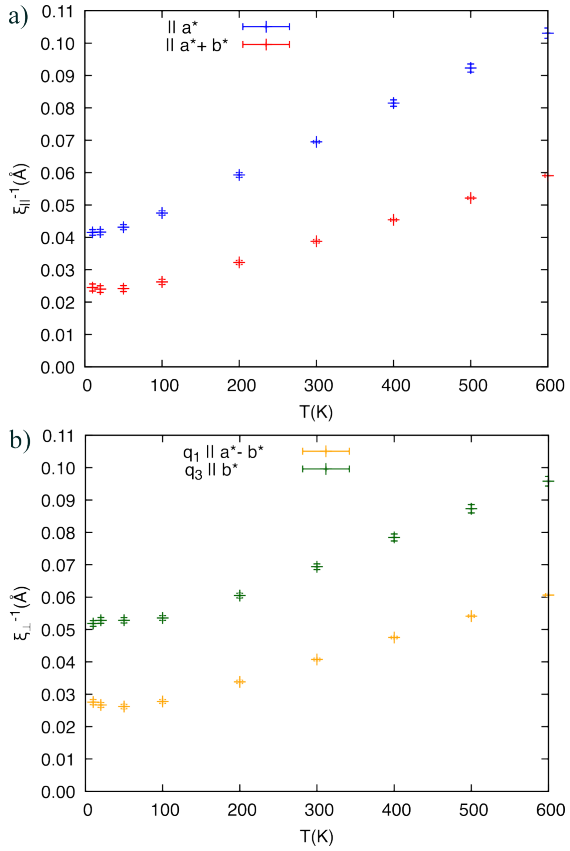

FIG. 13. Thermal dependence of the intra-chain (a) and inter-chain (b) electron-hole coherence length of the horizontal and diagonal chains in γ-Mo_4O_{11}.

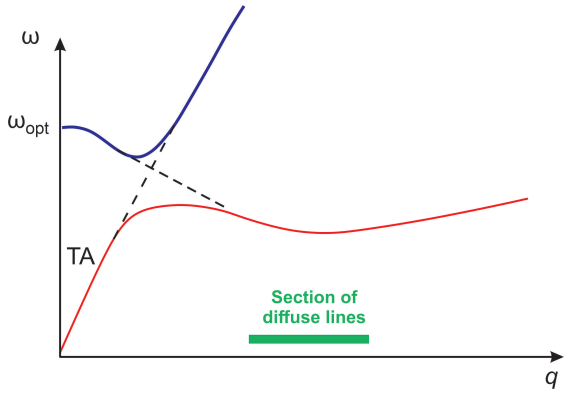

FIG. 14. Schematic representation of the hybridization between transverse acoustic (TA) and optical branches (ω_{opt}) leading to a valley of soft phonons in the q region materialized by the presence of diffuse lines in X-ray scattering.

electronic instability is not sufficient to drive the upper CDW ground state. In the RPA approximation the CDW instability occurs in fact for a maxima of $g(q)\chi(q)$, where $g(q)$ is the electron-phonon coupling. In other words, in addition to the electron-hole response one must also consider the q-dependence of the electron phonon-coupling[1] to really account for the CDW instability. In this section we consider the specificity of the electron phonon-coupling in 2D oxides and bronzes based on the available experimental results concerning the phonon spectrum of these materials. Not much is known about the phonon spectrum of the $MPTB_p$ and Mo_4O_{11} phases. However a phonon instability is unambiguously established and basically understood in the blue bronze, $K_{0.3}MoO_3$, which is a parent pseudo-1D CDW system.[5]

A significant electron-phonon coupling in these oxides and bronzes is achieved via the ferroelectric modes of deformation of segments built from several (m) corner-sharing octahedra (m= 6 in $P_4W_{12}O_{44}$, γ- and η-Mo_4O_{11}, and m= 4 in $K_{0.3}MoO_3$) which are the basic structural units of the metallic layers. The ferroelectric type instability of individual segments is revealed by the presence of a lattice of broad diffuse lines in X-ray diffuse scattering experiments for the blue bronze[51] and the $MPTB_p$[20,22] (however note that curiously such lines have not yet been detected in γ- and η-Mo_4O_{11}[17,20]). These lines correspond to the form factor of individual segments, as proven by simulation of the diffuse scattering in the $MPTB_p$.[20,52,53] They are due to a ferroelectric distortion of the segment with a relative shift of the Mo or W atoms inside each octahedron, as proven by the structural refinement of the CDW structure of the blue bronze[54] and the $MPTB_p$.[24–26] Two arrays of diffuse lines are clearly observed in the case of $MPTB_p$ because of the presence of two segment directions in their layers (see Fig. 17 below). In the case of the blue bronze there is only one type of diffuse lines because there is only one segment direction.

As reported longtime ago for ferroelectrics such as the cubic perovskites $BaTiO_3$, $KTaO_3$ and $KNbO_3$,[55] the coupling of a local polar deformation mode of the octahedra with a propagating transverse acoustic branch gives rise to a valley of soft phonons clearly evidenced by inelastic neutron scattering experiments (see also the case of the chain-like ferroelectric SbSi[56]). A somewhat similar scenario is observed in the blue bronze,[5,57] with however the difference that the q= 0 critical wave vector of ferroelectricity is shifted to $2k_F$ in the case of a CDW/Peierls instability. In the case of the m= 6 and m= 8 $MPTB_p$, recent inelastic X-ray scattering (IXS) studies[25,58] provide evidence for a broad valley of soft phonons (schematically represented in Fig. 14) for q wave vectors located inside the above quoted broad diffuse lines (in green in Fig. 14). As for the blue bronze,[5,57] this branch probably originates from the coupling of a polar optical mode (ω_{opt}) with a transverse acoustic (TA) branch.

The critical dynamics at the CDW/Peierls transition has only been extensively studied for the blue bronze.[5,59] It consists in a clear phonon frequency softening leading to the formation of a $2k_F$ sharp Kohn anomaly. In the m=6 $MPTB_p$ the IXS investigation reveals[58] only a weak frequency softening around q_1 when approaching the upper CDW transition (T_{CDW}= 120 K) without the development of a pronounced Kohn anomaly. The frequency

of this phonon mode, ∼4 meV at T_{CDW}, is comparable to the frequency of the higher energy amplitude mode detected at 5 K by fs spectroscopy.[60] Note also, in contrast with the non-critical phonon spectrum measured above T_{CDW}, that the frequency of several amplitude modes detected by fs spectroscopy exhibit a significant softening when approaching upwards the different CDW transitions of the m= 6 $MPTB_p$, as previously reported for the blue bronze.[59]

Not much is known about the critical CDW phonon dynamics of the Mo_4O_{11} Magnéli phases. First, no pretransitional diffuse lines revealing a preexisting valley of soft phonons associated with the diagonal chains has been detected by X-ray diffuse scattering in γ- and η-Mo_4O_{11}.[17,20] Second, amplitude modes detected below T_{CDW}=109 K by fs spectroscopy in η-Mo_4O_{11} were surprisingly found to be of constant frequency with temperature until T_{CDW}.[61] Finally a particular critical phonon dynamics should be expected if, as speculated on the basis of ARPES measurements, the spectral properties of η-Mo_4O_{11} bear typical characteristics of a Luttinger liquid.[62,63] In this case, one expects a stable Luttinger liquid only in the presence of a weak electron-phonon coupling.[64,65]

We thus conclude that, overall, the CDW lattice dynamics of m= 6 $MPTB_p$ shares many features with that of the blue bronze even if there are some significant differences. This suggests the possibility to build a common scenario to describe the CDW Peierls dynamics for these oxides and bronzes. On the basis of the presently available data, the Magnéli phases seem to exhibit similarities but also remarkable differences with the lower m members of the $MPTB_p$ family. For instance, despite having the same octahedral layers of the m= 6 $MPTB_p$ as well as the same topology of the band structure, FS and Lindhard response, there are remarkable differences in the physical behavior of the three compounds. One of the possible reasons is the larger band filling of the Magnéli phases. As noted before,[19,48] our calculations show that the partially filled conduction bands of these three systems are heavily concentrated on the inner part of the octahedral layers (i.e. the four inner octahedra of the unit highlighted in Fig. 1) and this is even more so in the Magnéli phases (89% of the Mo states in the filled portion of the conducting bands is associated with the two inner bands in γ-Mo_4O_{11} and 84% in $P_4W_{12}O_{44}$. See Fig. S2). Doubling the number of electrons in a relatively confined region should result with a substantial increase of the electronic repulsions which most likely play a more important role in the CDW lattice dynamics of the Magnéli phases and could be responsible for its Luttinger liquid behaviour.[62,63] Further work is urgently needed in order to generalize the scenario which is emerging for all these oxides and bronzes.

The nature of the critical CDW anomaly occurring at the upper CDW transition is unclear for the 2D molydnenum and tungsten bronzes and oxydes, while it is of the displacive type in the 1D blue bronze.[5] However, there is some evidence that the CDW transition in the m= 6 $MPTB_p$ is of the order-disorder type, although the amplitude of the PLD is equally small for all these compounds (∼0.05 Å). According to a recent theoretical study,[66] it appears that the nature of the CDW dynamics is not fixed by the amplitude of the PLD, as generally stated in the literature, but more likely by the spatial rate of decrease of the atomic potential setting the CDW. A large spatial decrease of this potential, described by s in Eq. (95) of reference [1] or $1/\alpha$ in reference [66], implies a large electron-phonon coupling. It causes a large effective pinning potential at the atomic scale which prevents the free sliding of the CDW modulation and favors an order-disorder type CDW dynamics. Such a realization is intimately connected with the strength of the chemical bonding pattern which in extreme cases leads to the formation of atomic clusters in the CDW ground state which strongly lock the modulation. Its relevance will be analyzed using the microstructure of $MPTB_p$ bronzes in the next section.

Note that the dynamical aspects of the CDW in $MPTB_p$ should be contrasted with those of rare earth tellurides, RTe_3, which are also hidden-nesting materials[1] and exhibit a displacive dynamics[67,68] associated with a very large PLD.[69,70] The displacive dynamics of the rare-earth tellurides should be associated with a small electron-phonon coupling (i.e. a small s value due to diffuse Te orbitals) and the absence of pinning effect allowing a non-linear conductivity.[71]

IX. INTERPLAY BETWEEN CDW GROUND STATES

$P_4W_{12}O_{44}$ as well as γ- and η-Mo_4O_{11} exhibit a high temperature CDW transition (120 and 109/100 K, respectively) characterized by the q_1 uniaxial modulation of Figs. 4, 10 and S4, respectively. At 60 K another CDW modulation, q_2 in Fig. 4, is stabilized for $P_4W_{12}O_{44}$. The last modulation involves only a single arm of the star of q_2 wave vectors[25] (see Fig. 15). No additional CDW transition is detected in γ-Mo_4O_{11} in contrast to η-Mo_4O_{11}. In that case a resistivity anomaly occurs at ∼30 K[21] that has been attributed to the nesting of the electron and hole pockets generated after the first CDW.[1,72] We remind that neither q_1 nor q_2 correspond to the strongest peak of the Lindhard response of $P_4W_{12}O_{44}$, and that the strongest response for γ-Mo_4O_{11}, q_3 in Fig. 10, is not related to any observed CDW transition.

It is also interesting to remark that the sequence of q_1 and q_2 CDW transitions is reversed between the m= 6 and m= 4 and 5 members of the $MPTB_p$ family.[20,23,24] This means that the gain of CDW free energy is close for both q_1 and q_2 modulations. Note also that the upper CDW transition of the m= 4 $MPTB_p$ involves a double q_2 modulation (q'_2 and q''_2 in Fig. 15)[24]. Thus, to understand the stabilization of the critical CDW modulation one must go beyond the electronic response and

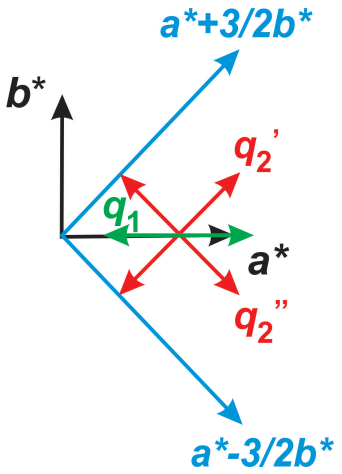

FIG. 15. Schematic representation of the (a^*,b^*) reciprocal layer of the MPTB$_p$, including the direction of the $a^*\pm3/2b^*$ diffuse lines (in blue) associated to the form factor of the two types of segments of m octahedra, together with the direction of the q_1 and double q_2 star CDW modulations activated in the upper CDW of the m=6 and m=4 members respectively. Note that only a single q_2 arm is activated in the intermediate CDW transition for the m= 6.

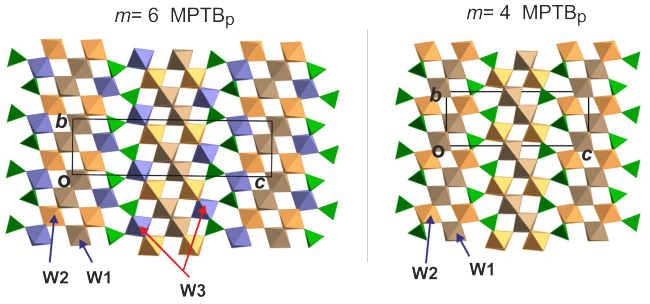

FIG. 16. Comparison of the crystal structures of the m= 6 and m= 4 MPTB$_p$ showing that the layer of the W1 and W2 octahedra, where the modulation occurs, is *protected* by the W3 octahedra in the m= 6 but not in the m= 4 case.

consider, at least qualitatively, the role of lattice degrees of freedom.

Let us first consider the double q_2 modulation of the upper CDW of the m= 4 MPTB$_p$. As shown in Fig. 15 these critical wave vectors (q_2' and q_2") are either aligned or perpendicular to the two sets of $2a^*\pm3b^*$directions of the pre-transitional diffuse lines (each direction is perpendicular to one type of segment). This means that the associated atomic modulation of the q_2 critical phonon should correspond either to a deformation in the longitudinal or transverse direction of the segment. As discussed above, the transverse segment deformation seems energetically favorable if only one chain direction is considered. However, because the $2q$ structure of the modulation, the two types of deformation occur simultaneously and should influence the CDW pattern on an equal footing. In this respect it has been proposed[24] that the $2q$ modulation should favor the formation of clusters of W atoms due to the overlap of deformed segments running in the two directions. In contrast, in oxydes and bronzes built from segments of six octaheda such as the m= 6 MPTB$_p$ as well as γ- and η-Mo_4O_{11}, the upper CDW modulation involves the q_1 uniaxial modulation along a^*. In this situation the longitudinal modulation wave vector is equally tilted with respect to the two directions of the segment (see Fig. 15).

At this point one must realize that the presence of the PO_4 (or MoO_4) tetrahedra introduce severe constraints to the development of structural modulations in the octahedral layers. It is thus important to remind that both in m= 6 MPTB$_p$ and the Mo_4O_{11} Magnéli phases the bands near the Fermi level concentrate electrons in the inner part of the octahedral layer (Fig. S2) made of the W1 and W2 octahedra (see Fig. 16). This is in agreement with the observation that the two upper CDWs of the m= 6 MPTB$_p$ practically do not affect the W3 octahedra.[25] As shown in Fig. 16 there is a significant difference between the m= 6 and the lower m members of the MPTB$_p$ family. For m= 6, the locus of the CDWs is protected by the W3 octahedra from the tensions generated by the layer connecting tetrahedra but not for m= 4. For the m=5 member half of the W3 protecting octahedra are missing. Note that the enhanced coupling in the m= 4 MPTB$_p$ causes the splitting of the FS, clearly shown in Fig. S7.

The longitudinal q_1 modulation must lead to a more uniform and favorable modulation. In the phases with units of six octahedra the outer octahedra (W3 in m=6 MPTB$_p$,[16] Mo2 in the Magnéli phases[46,47]) protect this modulation from the tetrahedra and the modulation can fully develop. However when the W3 octahedra do not occur, either partially for the m=5 or completely for the m= 4 members, the inter-layer connecting tetrahedra constrain the development of the longitudinal modulation and the system must find a different way to relieve the electronic instability. By choosing the $2q_2$ modulation the displacements within the octahedral segments may occur in different directions leading to the creation of octahedral clusters,[24,73] which do not occur in the uniaxial modulation. Both the q_1 and $2q_2$ modulations are different ways to relieve the electronic instability simultaneously in all layers keeping the orthorhombic symmetry. How the destruction of most of the FS associated with the diagonal chains along the $a \pm b$ directions can result from a uniaxial modulation along a can be understood from Fig. 17 where the inner layer of the W1 and W2 octahedra of the MPTB$_p$ is represented. The fragments of four octahedra in the diagonal directions have been highlighted with red or blue lines. Those with the same color are in the same step of the step-layers and the points where the different steps communicate, i.e. where the modulation is transmitted to the next step, are highlighted with green ellipses.

The high temperature CDW leaves a sizeable part of the FS. For instance, for the m= 6 MPTB$_p$ the uniax-

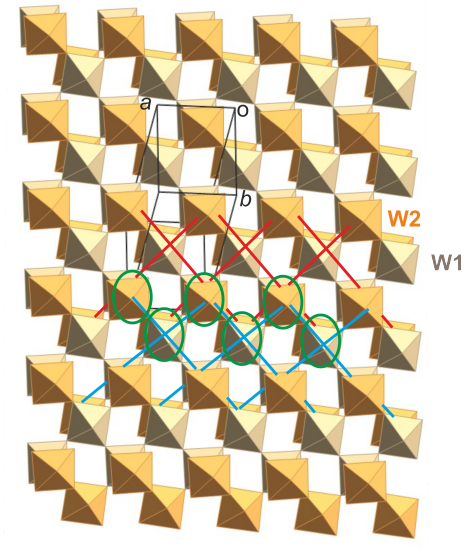

FIG. 17. Inner layer of the W1 and W2 octahedra in the MPTB$_p$. The fragments of four octahedra in the diagonal directions are highlighted with red or blue lines so that those with the same color are in the same step of the step-layer. The places where the modulation is transmitted to the next step along the diagonal direction are highlighted with green ellipses.

ial modulation does not affect the planes perpendicular to a^* so that most of these vertical portions of the FS will remain. In addition, some pockets coming from the crossing of the diagonal and horizontal planes will also remain. Thus, in principle the second transition should mostly affect the horizontal chains. In agreement with this idea the a^* component of the wave vector for second transition in m=6 MPTB$_p$ and η-Mo_4O_{11} is $2k_F$ of the horizontal chain. Note that since the planes of the Fermi surface associated with the horizontal chains are so flat, the nesting vector must have $2k_F^a$ as the a^* component but can have any b^* component. The wave vector of q_2 for m= 6 MPTB$_p$ fulfils this condition. It allows the destruction of large parts of the vertical planes and at least part of the pockets at the upper crossing of the vertical and diagonal planes of the FS. However note that since it involves a single arm of the star of the q_2 wave vectors, the orthorhombic symmetry is lost to become monoclinic and the two diagonal chains are no more equivalent.

That in η-Mo_4O_{11} the experimental wave vector of the second CDW modulation also contains a component along the c^* inter-layer direction suggests slightly stronger inter-layer interactions than in the m= 6 MPTB$_p$. This would be consistent with the different inter-layer connection in the two phases leading to the occurrence of pentagonal tunnels in m=6 MPTB$_p$ and γ-Mo_4O_{11} but hexagonal tunnels in η-Mo_4O_{11} (see the η-Mo_4O_{11} crystal structure in Fig. S3 in SI). The Lindhard response calculated for η-Mo_4O_{11} (see Figs. S4-S6 in SI) is very similar to that of γ-Mo_4O_{11}. However the intensity of the diffuse lines is weaker and we have verified that this is indeed the result of a slightly larger warping of the FS. In the m= 6 MPTB there is still a third CDW at lower temperature which according to its wave vector should probably nest the pockets at the lower crossing of the vertical and diagonal planes of the FS.

For the m=4 MPTB$_p$ the high temperature CDW (q= (0.330(5), 0.292(5), 0)[23,24]) is not of the uniaxial q_1 type because of the absence of protecting W3 octahedra. By adopting a $2q_2$ modulation the portion of the FS associated with the horizontal chains will be more severely destroyed and the FS pockets remaining will be more heavily based on the diagonal chains. This suggests that the low temperature modulation should be of the q_1 type which will nest these parts. The observed modulation is indeed of the q_1 uniaxial type, q= (0.340(5), 0, 0)[23,24]. In view of the previous comments it may be surprising that the wave vector of q_1 is now also $\sim 1/3\ a^*$ which is $2k_F$ of the horizontal chain. However, this is easy to understand because if the horizontal chain is 1/3-filled, as suggested by the a^* component of q_2, the two diagonal chains must also be 1/3-filled. In that case the two diagonal planes and the vertical plane of the FS must cross at the same point along the a^* direction (see Fig. S7 in SI) and the a^* component of q_1 and q_2 must be practically the same.

X. CONCLUDING REMARKS

The origin of the charge density wave instabilities in the MPTB$_p$ and Mo_4O_{11} Magnéli phases has been puzzling for a long time. The octahedral layers of these systems contain three different one-dimensional (1D) systems (two diagonal and one horizontal) associated with the three t_{2g} orbitals of the transition metal atoms. Because of the special topology of the layers the three 1D systems are practically independent even if they superpose. It is this property that led to the development of the *hidden-nesting* concept.[12] The present DFT study shows that the Lindhard response function of the $P_4W_{12}O_{44}$, γ- and η-Mo_4O_{11} contains three sets of intensity maxima associated with the horizontal and two diagonal 1D systems. Clear cusps, six for $P_4W_{12}O_{44}$ and four for γ- and η-Mo_4O_{11}, occur at the intersections of these intensity lines. The wave vector of the structural modulations associated with some of these cusps is in good agreement with the observed CDW wave vectors.

An in-depth study of the thermal dependence of intra- and inter-chain coherence lengths of the intensity lines provides useful information concerning the contribution of the different chains to the modulations. It is found that modulation in the diagonal chains is more favorable than in the horizontal chain. The same type of CDW wave vector is chosen by γ-Mo_4O_{11} and $P_4W_{12}O_{44}$ despite having a different band filling. This modulation is a longitudinal q modulation associated with the diagonal chains. The layers of these systems are built from groups of m= 6 corner-sharing octahedra. In contrast,

the high temperature modulation occurring in the lower m members (m= 4 and 5) of the $MPTB_p$ is due to a $2q$ modulation with different wave vector. The reason is that the modulation in these oxides and bronzes occurs in the inner part of the octahedral layer. In the m= 6 systems, this part is protected by additional octahedra from the inter-layer linking terahedra which introduce structural tensions. In the m=4 systems such protecting octahedra do not exist and the very uniform longitudinal q modulation is disfavoured. At lower temperatures a second (and occasionally a third) modulation destroys the unaffected portions of the FS.

The coupling of the electronic instability to the phonon spectra has been also discussed. The electron-phonon coupling in these systems occurs through ferroelectric deformation modes of the corner-shared octahedral m units. The coupling of a local polar deformation mode of the octahedra with a propagating transverse acoustic branch (q) gives rise to a valley of soft phonons clearly evidenced by inelastic X-ray scattering experiments in some $MPTB_p$. Among the two Magnéli phases the inter-layer coupling is found to be somewhat stronger in the η-Mo_4O_{11}. Concerning the critical dynamics at the CDW transition, $P_4W_{12}O_{44}$ shares many aspects with that of the blue bronze, suggesting the possibility to build a common scenario to describe the CDW Peierls dynamics for these oxides and bronzes. However, the Magnéli phases seem to exhibit similarities but also remarkable differences with the lower m members of the $MPTB_p$ family.

In hidden-nesting materials, several chains differing by the nature of their constituting orbitals spatially superpose. In conventional systems the chains are spatially separated and the inter-chain coupling, which is essentially of Coulomb type, is less efficient. The direct coupling in hidden-nesting materials may give rise to new interesting features. The comparison with another family of CDW materials, the rare-earth tellurides[43,44] is interesting. Although the real mechanism behind their CDW instability is still not completely clear,[1] Yao *et al*[45] discussed their CDW instabilities from the viewpoint of hidden-nesting. Using tight-binding arguments, they showed that for not very strong warping of the 1D FSs the actual nesting vector could change as a function of temperature. In the compounds studied here the wave vector of the modulation does not change at all with temperature. This means that the hidden 1D chains are strictly 1D (i.e. except for a very weak interaction at the crossing points, the FS components are very flat and thus transfer integral mediated inter-chain interactions between parallel chains do not play any significant role). In other words, the CDW in a given chain must be transmitted to another parallel chain either by direct Coulomb interactions, or indirectly via the polarization induced by an oblique chain so that unexpected new features can develop. For instance, our investigation reveals a new mechanism of diagonal coupling in $MPTB_p$ and Mo_4O_{11} Magnéli phases which could be relevant for others systems presenting the hidden-nesting mechanism such as the rare-earth tellurides. Clearly the term hidden-nesting should not be taken as simply meaning the superposition of classical 1D systems but suggesting the possibility of new and unexpected phenomena depending on the subtleties of the inter-chain coupling.

ACKNOWLEDGEMENTS

This paper owes much to numerous structural studies on 2D oxides and bronzes by P. Foury-Leylekian (Orsay) to whom we are very indebted. The authors also thank A. Minelli (Oak Ridge) for useful discussions concerning her IXS studies on the $MPTB_p$ and Elen Duverger-Nédellec (Bordeaux) for sharing the results of her structural studies. BG acknowledges computational resources provided by the Consortium des Équipements de Calcul Intensif (CÉCI), funded by the Fonds de la Recherche Scientifique (F.R.S.-FNRS) under Grant No. 2.5020.11 and the Tier-1 Lucia supercomputer of the Walloon Region, infrastructure funded by the Walloon Region under the grant agreement n°1910247. BG, MP and PO acknowledge support from Grant PID2022-139776NB-C62 funded by the Spanish MCIN/AEI/10.13039/501100011033 and by the ERDF, A way of making Europe and the Severo Ochoa program from Spanish MINECO (Grant no. CEX2021-001214-S). EC was supported by Grant PID2022-139776NB-C61 funded by the Spanish MCIN/AEI/10.13039/501100011033 and AEI through the Severo Ochoa MaTrans42 (CEX2023-0001263-S) Excellence Centre distinction. BG, MP, PO and EC acknowledge support from Generalitat de Catalunya (CERCA program and Grant 2021SGR01519).

[1] J.-P. Pouget and E. Canadell, Rep. Prog. Phys. **87**, 026501 (2024).
[2] P. Monceau, Adv. Phys. **61**, 325 (2012).
[3] J.-P. Pouget, C. R. Phys. **17**, 332 (2016).
[4] K. Rossnagel, J. Phys.: Condens. Matter **23**, 213001 (2011).
[5] B. Guster, M. Pruneda, P. Ordejón, E. Canadell, and J.-P. Pouget, Phys. Rev. Mat. **3**, 055001 (2019).
[6] B. Guster, M. Pruneda, P. Ordejón, E. Canadell, and J.-P. Pouget, J. Phys.: Condens. Matt. **33**, 485401 (2021).
[7] M. D. Johannes and I. I. Mazin, Phys. Rev. B **77**, 165135 (2008).
[8] P. Foury-Leylekian, J.-P. Pouget, Y.-J. Lee, R. M. Nieminen, P. Ordejón, and E. Canadell, Phys. Rev. B **82**, 134116 (2010).
[9] C. Schlenker, ed., *Low Dimensional Electronic Properties of Molybdenum Bronzes and Oxides*, Series: Physics and

Chemistry of Materials with Low-Dimensional Structures (Springer Netherlands, 1989).
[10] C. Schlenker, J. Dumas, M. Greenblatt, and S. van Smaalen, eds., *Physics and Chemistry of Low-Dimensional Inorganic Conductors*, NATO ASI Series B, Physics Vol. 354 (Plenum, New York, USA, 1996).
[11] J. Dumas, C. Schlenker, J. Marcus, and R. Buder, Phys. Rev. Lett. **50**, 757 (1983).
[12] M.-H. Whangbo, E. Canadell, P. Foury, and J.-P. Pouget, Science **252**, 96 (1991).
[13] P. Roussel, O. Pérez, and P. Labbé, Acta Cryst. B **57**, 603 (2001).
[14] M. Greenblatt, Int. J. Mod. Phys. B **7**, 3937 (1993).
[15] A. Magnéli, Acta Chem. Scand. **2**, 861 (1948).
[16] P. Labbé, M. Goreaud, and B. Raveau, J. Sol. State Chem. **61**, 324 (1986).
[17] H. Guyot, C. Schlenker, G. Fourcadot, and K. Konaté, Sol. State Comm. **54**, 909 (1985).
[18] E. Wang, M. Greenblatt, I. E.-I. Rachidi, E. Canadell, M.-H. Whangbo, and S. Vadlamannati, Phys. Rev. B **39**, 12969 (1989).
[19] E. Canadell and M.-H. Whangbo, Chem. Rev. **91**, 965 (1991).
[20] P. Foury and J.-P. Pouget, Int. J. Mod. Phys. B **7**, 3973 (1993).
[21] Y. Nogami, T. Kambe, N. Nagao, and K. Oshima, Synth. Met. **120**, 1049 (2001).
[22] P. Foury, P. P. Pouget, E. Wang, and M. Greenblatt, Europhys. Lett **16**, 485 (1991).
[23] A. Ottolenghi and J.-P. Pouget, J. Phys. I **6**, 1059 (1996).
[24] J. Lüdecke, A. Jobst, and S. van Smaalen, Europhys. Lett. **49**, 257 (2000).
[25] H. Duverger-Nedellec, *Transitions vers des états électroniques complexes et des structures super périodiques dans les Bronzes Mono Phosphates de Tungstène (https://theses.hal.science/tel-01941711v2)*, Ph.D. thesis, Normandie Université (2017).
[26] P. Roussel, P. Labbé, H. Leligny, D. Groult, P. Foury-Leylekian, and J.-P. Pouget, Phys. Rev. B **62**, 176 (2000).
[27] C. Guyot, H. anf Schlenker, J. P. Pouget, R. Ayroles, and C. Roucau, J. Phys. C **18**, 4427 (1985).
[28] E. Sandré, P. Foury-Leylekian, S. Ravy, and J.-P. Pouget, Phys. Rev. Lett. **86**, 5100 (2001).
[29] P. Hohenberg and W. Kohn, Phys. Rev. **136**, B864 (1964).
[30] W. Kohn and L. J. Sham, Phys. Rev. **140**, A1133 (1965).
[31] J. M. Soler, E. Artacho, J. D. Gale, A. García, J. Junquera, P. Ordejón, and D. Sánchez-Portal, J. Phys.: Condens. Matter **14**, 2745 (2002).
[32] E. Artacho, E. Anglada, O. Diéguez, J. D. Gale, A. García, J. Junquera, R. M. Martin, P. Ordejón, J. M. Pruneda, D. Sánchez-Portal, and J. M. Soler, J. Phys.: Condens. Matter **20**, 064208 (2008).
[33] A. García, N. Papior, A. Akhtar, E. Artacho, V. Blum, E. Bosoni, P. Brandimarte, M. Brandbyge, J. I. Cerdá, F. Corsetti, R. Cuadrado, V. Dikan, J. Ferrer, J. Gale, P. García-Fernández, V. M. García-Suárez, S. García, G. Hihs, S. Illera, R. Korytár, P. Koval, I. Lebedeva, L. Lin, P. López-Tarifa, S. G. Mayo, S. Mohr, P. Ordejón, A. Postnikov, Y. Pouillon, M. Pruneda, R. Robles, D. Sánchez-Portal, J. M. Soler, R. Ullah, V. Wenzhe Yu, and J. Junquera, J. Chem. Phys. **152**, 204108 (2020).
[34] J. P. Perdew, K. Burke, and M. Ernzerhof, Phys. Rev. Lett. **77**, 3865 (1996).
[35] N. Troullier and J. L. Martins, Phys. Rev. B **43**, 1993 (1991).
[36] L. Kleinman and D. M. Bylander, Phys. Rev. Lett. **48**, 1425 (1982).
[37] E. Artacho, D. Sánchez-Portal, P. Ordejón, A. García, and J. M. Soler, Phys. Status Solidi (b) **215**, 809 (1999).
[38] H. J. Monkhorst and J. D. Pack, Phys. Rev. B **13**, 5188 (1976).
[39] E. Canadell and M.-H. Whangbo, Phys. Rev. B **43**, 1894 (1991).
[40] D. Boskovic, *Electronic properties of organic semiconductors and low-dimensional materials (http://hdl.handle.net/10803/456582)*, Ph.D. thesis, Universitat Autònoma de Barcelona (2017).
[41] K. R. Locherer, I. P. Swainson, and E. K. H. Salje, J. Phys.: Condens. Matter **11**, 4143 (1999).
[42] S. Paul, A. Ghosh, T. Sato, D. D. Sarma, T. Takahashi, E. Wang, M. Greenblatt, and S. Raj, Europhys. Lett. **105**, 46003 (2014).
[43] E. DiMasi, M. C. Aronson, J. F. Mansfield, B. Foran, and S. Lee, Phys. Rev. B **52**, 14516 (1995).
[44] K. Y. Shin, J. Laverock, Y. Q. Wu, C. L. Condron, M. F. Toney, S. B. Dugdale, M. J. Kramer, and I. R. Fisher, Phys. Rev. B **77**, 165101 (2008).
[45] H. Yao, J. A. Robertson, E.-A. Kim, and S. A. Kivelson, Phys. Rev. B **74**, 245126 (2006).
[46] M. Ghedira, H. Vincent, and M. Marezio, J. Solid St. Chem. **56**, 66 (1985).
[47] L. Kihlborg, Arkiv Kemi **21**, 365 (1963).
[48] E. Canadell, M.-H. Whangbo, C. Schlenker, and C. Escribe-Filippini, Inorg. Chem. **28**, 1466 (1989).
[49] C. M. Varma and W. Weber, Phys. Rev. Lett. **39**, 1094 (1977).
[50] F. Flicker and J. van Wezel, Nat. Commun. **74**, 245126 (2015).
[51] J. P. Pouget, S. Kagoshima, C. Schlenker, and J. Marcus, J. Physique Lettres **44**, L113 (1983).
[52] P. Foury, J. P. Pouget, Z. L. Teweldemehin, E. Wang, M. Greenblatt, and D. Groult, J. Phys. IV **3**, 133 (1993).
[53] P. Foury, J. P. Pouget, Z. L. Teweldemehin, E. Wang, and Greenblatt, Synth. Met. **56**, 2605 (1993).
[54] W. J. Schutte and J. L. de Boer, Acta Crystallogr. B **49**, 579 (1993).
[55] R. Comès and G. Shirane, Phys. Rev. B B **5**, 1886 (1972).
[56] J. P. Pouget, S. M. Shapiro, and K. Nassau, J. Phys. Chem. Solids **40**, 267 (1979).
[57] J. P. Pouget, E. Canadell, and B. Guster, Phys. Rev. B **103**, 115135 (2021).
[58] A. Minelli, *Les bronzes monophosphate de tungstène et l'antimoine: l'interaction entre l'instabilité de "framework" et le couplage électron-phonon (https://theses.hal.science/tel-02271297)*, Ph.D. thesis, Université Grenoble Alpes (2018).
[59] J. P. Pouget, B. Hennion, C. Escribe-Filippini, and M. Sato, Phys. Rev. B **43**, 8421 (1991).
[60] L. Stojchevska, M. Borovšak, P. Foury-Leylekian, J.-P. Pouget, T. Mertelj, and D. Mihailovic, Phys. Rev. B **96**, 035429 (2017).
[61] M. Borovšak, L. Stojchevska, P. Sutar, T. Mertelj, and D. Mihailovic, Phys. Rev. B **93**, 125123 (2016).
[62] G.-H. Gweon, S.-K. Mo, J. W. Allen, C. R. Ast, H. Höchst, J. L. Sarrao, and Z. Fisk, Phys. Rev. B **72**, 035126 (2005).
[63] X. Du, L. Kang, Y. Y. Lv, J. S. Zhou, X. Gu, R. Z. Xu, Q. Q. Zhang, Z. X. Yin, W. X. Zhao, Y. D. Li, S. M. He,

D. Pei, Y. B. Chen, M. X. Wang, Z. K. Liu, Y. L. Chen, and L. X. Yang, Nature Physics **19**, 40 (2023).
[64] J. Voit, Rep. Prog. Phys. **58**, 977 (1988).
[65] J. Voit and H.-J. Schulz, Phys. Rev. B **37**, 10068 (1988).
[66] O. Cépas and P. Quémerais, "Aubry transition with small distortions," arXiv:2405.01878v1 [cond-math.other], 3 May 2024.
[67] M. Maschek, S. Rosenkranz, R. Heid, A. H. Said, P. Giraldo-Gallo, I. R. Fisher, and F. Weber, Phys. Rev. B **91**, 235146 (2015).
[68] M. Maschek, D. A. Zocco, S. Rosenkranz, R. Heid, A. H. Said, A. Alatas, P. Wamsley, I. R. Fisher, and F. Weber, Phys. Rev. B **98**, 094304 (2018).
[69] C. D. Malliakas, S. J. L. Billinge, H. J. Kim, and M. G. Kanatzidis, J. Am. Chem. Soc. **127**, 6510 (2005).
[70] H. J. Kim, C. D. Malliakas, A. T. Tomic, S. H. Tessmer, M. G. Kanatzidis, and S. J. L. Billinge, Phys. Rev. Lett. **96**, 226401 (2006).
[71] A. A. Sinchenko, P. Lejay, and P. Monceau, Phys. Rev. B **85**, 241104(R) (2012).
[72] M.-H. Whangbo and E. Canadell, Acc. Chem. Res. **22**, 375 (1989).
[73] J. Lüdecke, A. Jobst, S. Geupel, and S. van Smaalen, Phys. Rev. B **64**, 104105 (2001).